



Single-atom Nb anchored on graphitic carbon nitride for boosting electron transfer towards improved photocatalytic performance

Jianmin Luo ^{a,b,*}, Haonan Han ^{a,b}, Xinglei Wang ^b, Xiuzhen Qiu ^a, Bin Liu ^a, Yinlong Lai ^a, Xiaoyuan Chen ^a, Ruimin Zhong ^a, Lei Wang ^{c,**}, Chuanyi Wang ^d

^a Guangdong Provincial Key Laboratory of Utilization and Conservation of Food and Medicinal Resources in Northern Region, School of Chemistry and Civil Engineering, Shaoguan University, Shaoguan 512005, PR China

^b Key Laboratory of Pollutant Chemistry and Environmental Treatment, College of Chemistry and Environmental Science, Yili Normal University, Yining 835000, PR China

^c Department of Chemical Engineering, University of Minnesota-Duluth, Duluth, MN 55812, USA

^d Guangzhou Institute of Industrial Intelligence, Guangzhou 511400, PR China



ARTICLE INFO

Keywords:

Nb single-atom
Carbon nitride
Nb-C bond
Nitrogen defect
Photocatalytic activity

ABSTRACT

Single-atom Nb anchored on g-C₃N₄ was prepared by facile thermal polymerization. Compared with pure g-C₃N₄, optimized Nb-anchoring samples exhibited excellent CO and CH₄ yield and higher photocatalytic oxidation efficiency in degrading amoxicillin (AMX). Combining DFT calculations and experimental results, the enhanced photocatalytic performance was attributed to anchored single-atom Nb in terms of Nb-C and the formation of N defects. Anchoring with single-atom Nb contributed to the formation of N defects in g-C₃N₄, inducing the formation of polarized Nb-C bonds with high conductivity accelerating the directional transfer of photogenerated electrons and holes. Moreover, this restrained the relatively high charge carrier recombination rate of g-C₃N₄. Additionally, N defects with solitary electrons could enhance the charge density and serve as active centers for a photocatalytic reaction. The present work underlines the importance of the synergistic effect of anchoring Nb and simultaneously generating N defects for developing a new generation of g-C₃N₄-based photocatalysts.

1. Introduction

In recent years, amoxicillin (AMX) has been a widely used β-lactam antibiotic widely detected in groundwaters. Even trace amounts of AMX can raise a series of issues, including the emergence of antibiotic resistance genes and chronic toxic effects [1,2]. Unfortunately, conventional biodegradation is inefficient in removing these pollutants [3]. Over the past few years, many strategies have been proposed to address this issue [3–5]. Among these, photocatalysis is an economical, effective, and environmentally friendly method that shows wide applicability for removing pollutants. As well known that the carbon dioxide (CO₂) can be produced during the mineralization of amoxicillin [3,4,6,7]. Besides, excessive CO₂ emissions are the main cause of the greenhouse effect. Previous reports have shown that photocatalytic reduction of CO₂ can produce combustible gases such as CO and CH₄, which not only solve air pollution but also help to solve energy problems. The stability of the CO₂

is strong, so the photocatalyst, which could produce a lot of electrons, is needed to reduce it. Therefore, the design of a photocatalyst with strong oxidation and reduction ability is the main approach to solve the environmental pollution and energy crisis.

Among semiconductor-based photocatalysts, graphitic carbon nitride (g-C₃N₄) as a polymer semiconductor has attracted widespread attention due to its unique electronic structure, nontoxicity, low cost, and good chemical stability. Nevertheless, the applicability of g-C₃N₄ is hindered by the fast recombination rate of photogenerated electron-hole pairs, low electrical conductivity, and poor visible light absorption. Besides, the high photocatalytic activity depends on photogenerated charge carriers' efficient separation and migration efficiency. Therefore, constructing a novel and efficient g-C₃N₄-based photocatalyst is highly desired [8,9]. Fortunately, as a flexible material of g-C₃N₄ is easy to be modified. By improving the energy conversion efficiency of catalysts to visible light and enhancing the charge transfer ability, the performance

* Corresponding author at: Guangdong Provincial Key Laboratory of Utilization and Conservation of Food and Medicinal Resources in Northern Region, School of Chemistry and Civil Engineering, Shaoguan University, Shaoguan 512005, PR China.

** Corresponding author.

E-mail addresses: xxyljm@163.com (J. Luo), wan00818@d.umn.edu (L. Wang).

of g-C₃N₄-based photocatalysts can be improved.

Single-atom catalysts (SACs) can maximize the atom utilization efficiency and change the atomic and electronic structures of the active sites [10–12]. Thus, they have gradually become a research hotspot in the photocatalysis field in recent years. Unlike traditional nanoclusters, in theory, there is no mutual contact between adjacent atoms for the metals in SACs. The unique electronic structure exists between the single metal atom and the supported photocatalyst, which can accelerate charge transfer and prolong the lifetime of carriers [13–15]. In short, SACs would enhance photocatalytic activity and be an economical and efficient catalyst design concept.

On the other hand, single-atom anchoring of transition metals could improve the photocatalytic performance of g-C₃N₄ [16,17]. Meanwhile, abundant N defects produced by the thermal polymerization method (in-situ synthesis) in the amorphous g-C₃N₄ [18–20] are very easy to coordinate with the single metal atoms and anchor the single metal atoms [21–23]. Transition atom anchored has also been reported as an efficient method for improving the visible-light photocatalytic activity of g-C₃N₄. However, most of the monatomic modified g-C₃N₄ are modified with precious metals up to now. Although single atoms of precious metals such as gold, platinum, silver, and palladium have unique electrical conductivity, they are expensive, difficult to anchor in large quantities, and easy to form clusters. Developing a cheap single-atom photocatalyst with excellent electrical conductivity is imperative to realize the rational use of resources and energy. This is also in line with the current concept of human development. Nb, a metal with excellent performance and low cost, is widely used in modifying materials. Moreover, it is reported that most compounds of Nb and N or C have excellent electrical conductivity [24]. Importantly, the radius of the Nb is smaller than layer spacing and the triazine ring radius of g-C₃N₄, and the radius of Nb⁵⁺ and Nb⁴⁺ is approximated that of N atoms. Meanwhile, Nb's unique d orbital (4d⁴5 s¹) will also provide many impurity bands for the g-C₃N₄. When single-atom Nb is anchored on the surface of g-C₃N₄, it is easy to replace N vacancy, forming coordination with C atoms.

In this study, a simple thermal polymerization method was used to prepare the single-atom Nb anchored on g-C₃N₄ (CNNb) with a large number of N defects. A series of characterizations and density functional theory (DFT) calculations proved the generation of N defects and the formed Nb-C bond. N defects can accelerate the transformation of excitons into photogenerated carriers, providing more channels for charge transfer and promoting redox semi-reaction. The results of photocatalytic redox performance demonstrated that the CNNb0.06 sample has the strongest AMX oxidation ability and the best CO₂ reduction activity. Through photoelectronic properties and DFT calculations, the as-formed Nb-C transfers the charge inspired from the conduction band in a form like a "high-speed rail". After irradiation with visible light, Nb as an electron absorbing site promotes the photogenerated electrons produced on LUMO to migrate to the valence band along C-Nb and accumulate near Nb, which increases the number of photogenerated electrons on the surface of CNNb0.06. Meanwhile, the increase of electron density and the enhancement of adsorption improve the ability of the CNNb0.06 system to produce •O₂[−] and reduce CO₂. Additionally, Nb's variable valence introduces the single-electron reduction of H₂O₂, which produces •OH for the CNNb0.06 catalyst. The single-atom anchored on g-C₃N₄ obtained strong oxidation and reduction properties with the increased reactive oxygen species concentration and charge transfer ability.

2. Experimental

2.1. Preparation of photocatalysts

All chemicals were of analytical grade and used without further purification. g-C₃N₄ was prepared by annealing melamine at a high temperature. Typically, 4 g of melamine was placed in a covered

crucible and heated in a muffle furnace at 520 °C for 2 h at a heating rate of 10 °C min^{−1}. After cooling to room temperature, the product was ground into fine powder to yield g-C₃N₄. For comparison purposes, synthesis of g-C₃N₄ with N defects (Nv-CN) was performed with 4 g of melamine, which was reheated to 520 °C for 2 h at a rate of 10 °C min^{−1} in an N₂ atmosphere. After the sample was cooled naturally, the yellow powder was collected to obtain Nv-CN. The single-atom Nb-anchored g-C₃N₄ was prepared by annealing a mixture of g-C₃N₄ and niobium oxalate powder. The preparation process of CNNbx (x = 0.02, 0.06, 0.1, and 0.2) was detailed in Text S1 of Supporting Information (SI).

2.2. Characterization of photocatalysts

The parameters of the test and characterization processes are detailed in Text S2 of SI.

2.3. Photocatalytic CO₂ reduction

The photocatalytic experiments were carried out in a vacuum reaction system with a total volume. In the center of the reaction cell, a 50 mg sample was uniformly dispersed on a 2.5 cm × 2.5 cm glass panel. Then, 0.8 mL of deionized water was injected into the reactor as steam. After evacuating the system, 0.8 mPa CO₂ (99.999%) was introduced, and a 300 W Xe lamp was employed as the light source. The incident light intensity in the reaction was measured to be 450 mW cm^{−2} (five-point measurement, the Sorebo light intensity meter). The concentrations of gaseous products in the effluent gas were periodically sampled. They then used a gas chromatograph (Shimadzu Co., Japan) with two gas analysis channels to measure its compositions: one channel for the analysis of CO and CO₂ and the other for measuring CH₄.

2.4. The evaluation of photocatalytic removal of AMX

The photocatalytic performances of g-C₃N₄ CNNb0.02, CNNb0.06, CNNb0.1, and CNNb0.2 were tested by the degradation of AMX solution under visible light irradiation. In each test, a 0.1 g sample was evenly dispersed in 100 mL AMX aqueous solution (5 mg L^{−1}), which was then stirred in the dark for 0.5 h to achieve the adsorption-desorption equilibrium. The stirred solution was irradiated by a simulated visible light source (300 W xenon lamp). 5 mL of turbid liquid was extracted from the suspension every 6 min, and the supernatant was separated by centrifugation. The column temperature was 25 °C, and the detection wavelength was 254 nm. The volume ratio of 0.05 M KH₂PO₄ aqueous solution to acetonitrile in the mobile phase was 97:3, the flow rate was 1 mL min^{−1}, and the sample volume was 20 μL for each injection. The degradation efficiency and total organic carbon (TOC) content were calculated by Formula (1):

$$\eta = 1 - (C/C_0) \quad (1)$$

where C represents the supernatant concentration of AMX or TOC after visible light irradiation for a certain length of time, and C₀ represents the AMX or TOC concentration after achieving equilibrium in the dark.

2.5. Characterizing the solid phase with X-ray absorption fine structure (XAFS) analyses

The Nb K-edge analysis was performed with Si (111) crystal monochromators at the BL14W1 beamlines at the Shanghai Synchrotron Radiation Facility (SSRF) (Shanghai, China). Before the analysis at the beamline, samples were pressed into thin sheets of 1 cm in diameter and sealed using Kapton tape film. The XAFS spectra were recorded at room temperature using a 4-channel Silicon Drift Detector (SDD) Bruker 5040. Fe K-edge extended X-ray absorption fine structure (EXAFS) spectra were recorded in transmission mode. Negligible changes in the line shape and peak position of Fe K-edge XANES spectra were observed

between two scans taken for a specific sample. The XAFS spectra of these standard samples (Nb-foil and Nb_2O_5) were recorded in transmission mode. The spectra were analyzed by the software codes Athena and Artemis.

2.6. Detection of hydroxyl radical ($\bullet\text{OH}$) and H_2O_2

The process of hydroxyl radical ($\bullet\text{OH}$) investigations and the determination process of H_2O_2 are detailed in Texts S2 and S3 of SI.

2.7. Photoelectrochemical experiments

The details regarding the photoelectrochemical experiments are explained in Text S5 of SI.

2.8. Theoretical calculations

The parameters of DFT calculations are defined in Text S6 of SI.

3. Results and discussion

3.1. Composition and structure analysis

The element composition and content of the CNNb0.06 sample were investigated by EDS (Fig. 1a), showing that the elements of C, N, and Nb coexisted in the system. The elemental composition of CNNb0.06 was further investigated by elemental mapping. As depicted in Fig. 1b–d, the elements looked evenly distributed in the samples, consistent with the EDS results. The phase structures of the CNNb0.06 system and g-C₃N₄ were characterized by transmission electron microscopy (TEM) and high-resolution transmission electron microscopy (HRTEM). The g-C₃N₄ sample presented an irregular shape with layered mesostructure as determined by Fig. 1e and f. On the other hand, many holes were randomly distributed around the surface of the CNNb0.06 system (Fig. 1g and h). The destruction of the original crystal phase of g-C₃N₄ by Nb anchoring accelerated the generation of defects on the CNNb0.06 surface in the process of thermal polymerization. Meanwhile, the distortion of the lattice increased the specific surface area of samples. Additionally, no crystalline phase can be found on the CNNb0.06 surface (Fig. 1h). To further confirmed the absence of agglomerated Nb

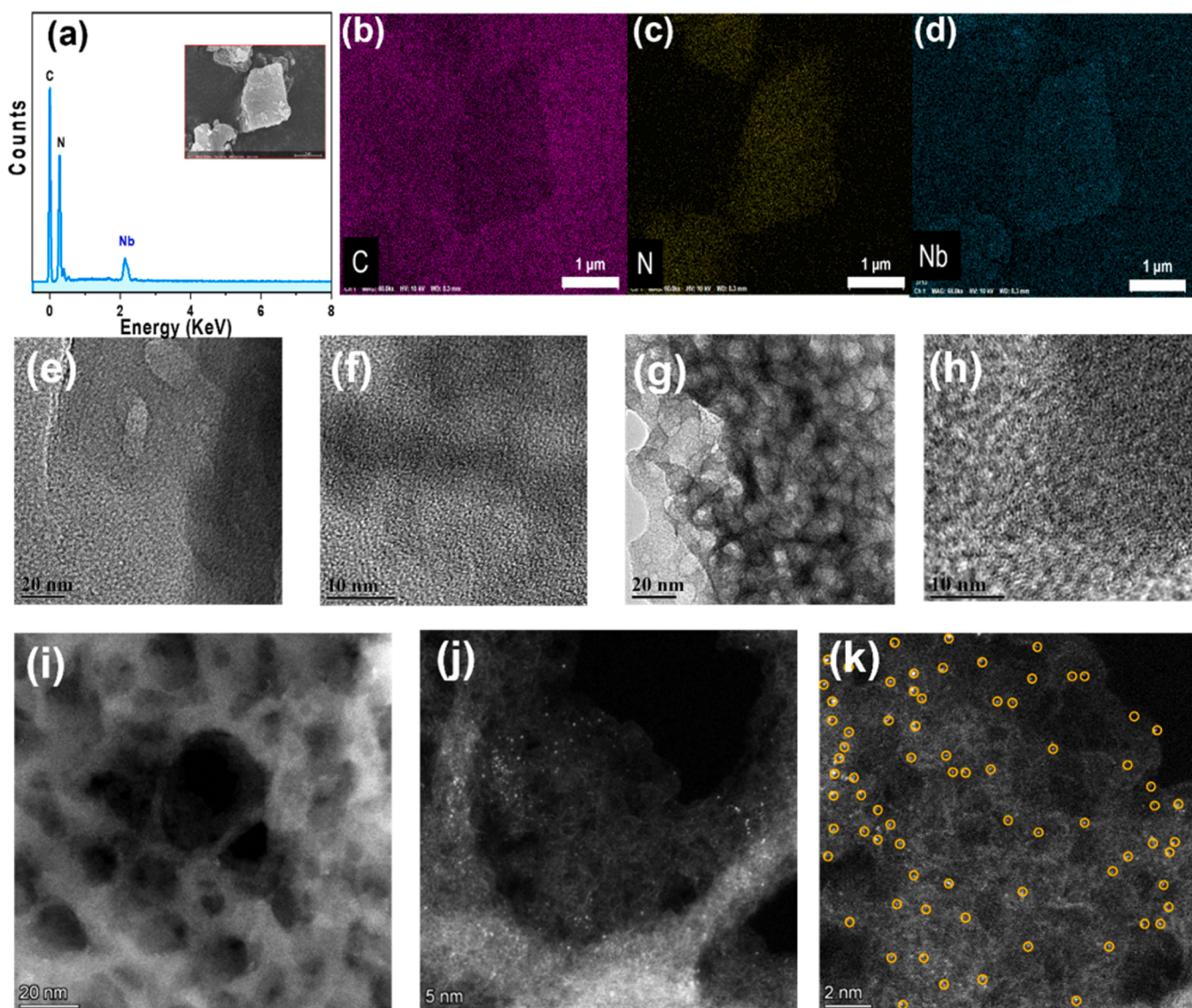


Fig. 1. The EDS spectra (a); elemental mapping images for C (b), N (c), and Nb (d) elements of CNNb0.06; TEM (e) and HRTEM (f) images of g-C₃N₄; TEM (g) and HRTEM (h) images of CNNb0.06; the HAADF-STEM images (i ~ k) of CNNb0.06.

nanoparticles in CNNb0.06, the high-angle annular dark-field scanning TEM (HAADF-STEM) was carried out (Figs. 1i–k and S1) [25]. Fig. 1k showed that the bright spots corresponding to Nb atoms were distributed uniformly on the surface of based g-C₃N₄. Moreover, the size of Nb on g-C₃N₄ for this sample is far less than 2 Å, which proved the successful preparation of the single-atom Nb-anchored g-C₃N₄ [10,26,27].

Moreover, the crystal structures of g-C₃N₄ and CNNb systems were first investigated by XRD. As shown in Fig. 2a, each catalyst revealed two diffraction peaks at 2θ values of 13.0° and 27.4°, corresponding to (100) and (002) crystal planes. Hence, all samples were based on g-C₃N₄-modified materials [28]. Also, diffraction peaks related to Nb species were not observed, meaning Nb was well dispersed in the catalysts. However, the increase in the Nb anchoring amount declined the intensity of diffraction peaks at 13.0° and 27.4°, implying damage to the crystal phase of the system and the formation of more defects with lower crystallinity.

The chemical structures and functional groups of the as-synthesized samples were further studied by FTIR. As exhibited in Fig. S2, all samples revealed obvious peaks at approximately 810 cm⁻¹, 1240 ~ 1650 cm⁻¹, and 3000 ~ 3400 cm⁻¹ [29], assigned to the breathing mode of triazine units, stretching vibrations mode of modes of C-N and C=N heterocycles, N-H and O-H [30,31], respectively. The characteristic peaks of different samples remained unchanged. The main characteristic peaks of C-N hetero-cycles with triazine units of g-C₃N₄ were detectable in all photocatalysts, demonstrating the existence of Nb in CNNb photocatalysts in terms of anchoring.

The chemical valence of each element in g-C₃N₄ and CNNb0.06 were further investigated by XPS. As depicted in Fig. 2b, elements C, N, and O were detected in spectra of g-C₃N₄ and CNNb0.06. Compared to pure g-C₃N₄, an additional peak can be observed in the CNNb0.06, corresponding to Nb 3d, indicating the successful introduction of Nb into the g-C₃N₄. The C 1 s XPS spectra of g-C₃N₄ and CNNb0.06 are displayed in Fig. 2c. The peaks at 284.8 eV and 288.4 eV were ascribed to adventitious carbon from the instrument (C-C), and C bonded to N by sp² hybridized (N = C-N) in triazine units, respectively [32]. It is worth noting

that the peak at 284.3 eV attributed to C-Nb was also found in CNNb0.06. In Fig. 2d, the g-C₃N₄ showed three characteristic peaks of N 1 s at 399.08 eV, 400.23 eV, and 401.58 eV, assigned to sp² hybridized aromatic N bonded with carbon atoms of (C-N = C), the bridge N in triazine (N-C₃) and surface uncondensed amino groups bound to hydrogen (C-NH₂), respectively. Hence, combined with the high-resolution spectra of C 1 s and N 1 s, it can be concluded that the CNNb0.06 system still retained the basic triazine structure of g-C₃N₄, consistent with the results shown by FTIR. It is worth mentioning that the N-(C)₃ and C-N = C structure characteristic peaks gradually moved in the direction of high binding with the single atom Nb anchoring, mainly because N-C₃ and C-N = C lost electrons., indicating that the Nb atoms might have replaced N and C to form Nb-C bonds. It is speculated that Nb is more inclined to replace the bridged nitrogen site, because the binding energy of N-C₃ structure changes greatly.

The XPS spectra of Nb 3d of as-prepared samples are shown in Fig. 2e. The spectra of CNNb0.06 displayed four characteristic peaks, the two peaks located at 207 eV and 209.8 eV were assigned to Nb⁴⁺, while the other two peaks at 207.6 eV and 210.5 eV corresponded to Nb⁵⁺[33]. Furthermore, the CNNb0.02, CNNb0.1 and CNNb0.2 were characterized by Nb 3d XPS to determine the existence status of Nb in samples with the increase of anchor quantity. As shown in Figs. 2e and S3a, Nb exists in the form of + 5 and + 4 valences in all CNNbx samples. And the content of + 5 valence Nb increases gradually with the increase of Nb anchored quantity. Combined with the results of HAAADF-STEM, it was concluded that there was no formation of Nb nanoparticles. Furthermore, the samples were further characterized by O 1 s XPS. The Figs. 2f and S3b were exhibited that all samples have a characteristic peak representing adsorbed oxygen (531.8–532.8 eV), and there is no characteristic peak represented to lattice oxygen (529.3–530.5 eV) and C-O-C bond (531.4 eV) after fitting. This preliminarily indicates that there is no Nb-O bond in the system of Nb anchored on g-C₃N₄.

Moreover, the interlayer spacing (3.16 Å) and cavity size (4.74 Å) of g-C₃N₄ were much bigger than the diameter of the Nb ion (0.69 Å or 0.23 Å). Thus, Nb atoms can be inserted into layers and triazine ring

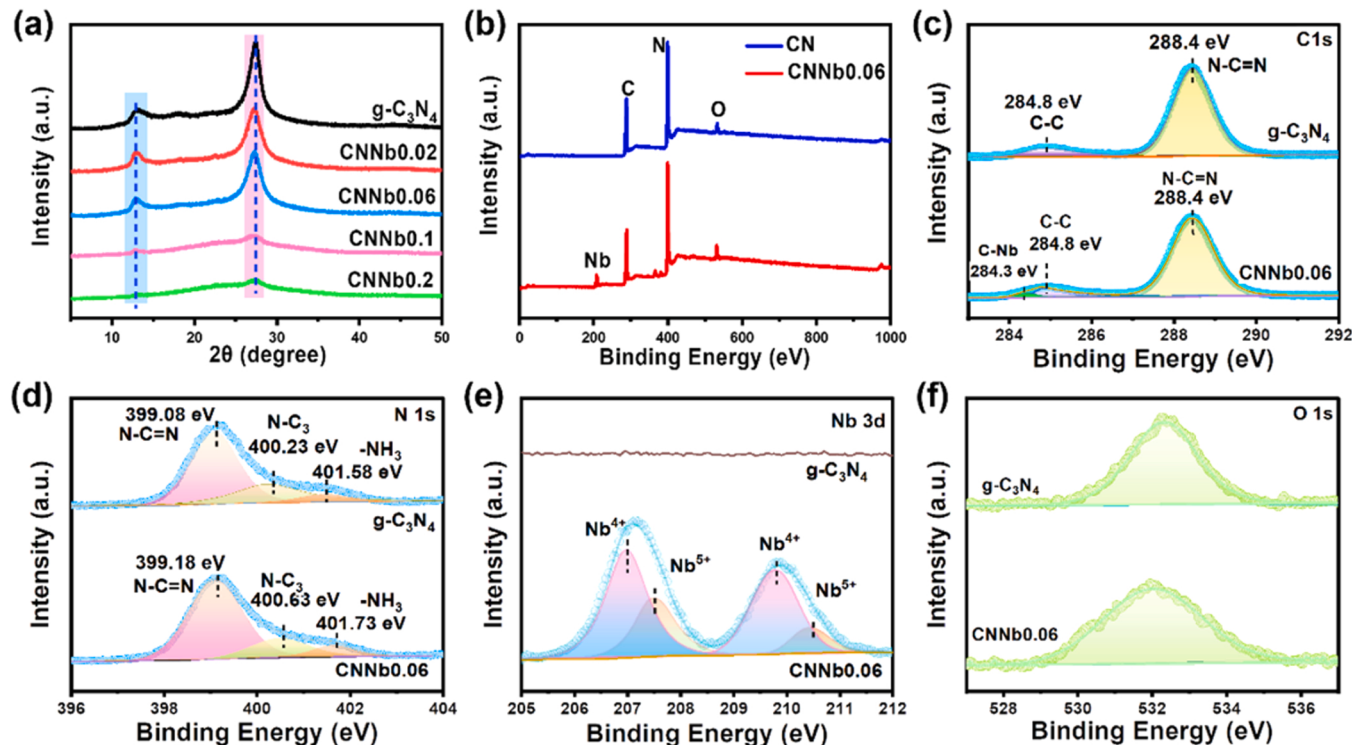


Fig. 2. The X-ray diffraction (XRD) patterns (a); survey XPS spectra (b) of g-C₃N₄ and CNNb0.06; the high resolutions C 1s (c), N 1s (d), Nb 3d (e) and O 1s (f) XPS spectra of g-C₃N₄ and CNNb0.06.

cavities of $\text{g-C}_3\text{N}_4$. Based on the outer electron layer configuration of Nb ($4 \text{d}^4 5 \text{s}^1$) [34], Nb can lose not only one electron from the 5s orbital but also an electron from the 4d orbital during the formation of the compound [35]. The radius of Nb^{4+} and Nb^{5+} is close to the N or C atomic radii, which both possess lone pairs of electrons. Thus, Nb may replace C site or N site when N or C vacancies are formed, and form a coordination bond with C or N [21,36].

The Nb species' electronic states and coordination environments in CNNb0.06 were further examined by synchrotron radiation-based XANES and EXAFS characterizations at Nb K-edge. The E-space spectra show that the absorption edge of CNNb0.06 was located at the

position between Nb foil and Nb_2O_5 (Fig. 3a), revealing that the valence of Nb existed in CNNb0.06 with between 0 to +5 [37,38]. In addition, the absorption edge of the sample was close to Nb_2O_5 , which proves that Nb atoms exist mainly in the form of +5 valence. This result consisted of XPS analysis. As shown in Fig. 3b, the main peak corresponding to CNNb0.06 moved forward relative to Nb_2O_5 in the first coordination shell, resulting from the interaction between Mo species and coordination atoms (such as C or N) with less electronegativity than O [39,40]. Meanwhile, no peak representing Nb-Nb was found in CNNb0.06, indicating that the single atom of Nb is uniformly dispersed in the system. Besides, as displayed in Table S2 and Fig. 3c, quantitative EXAFS

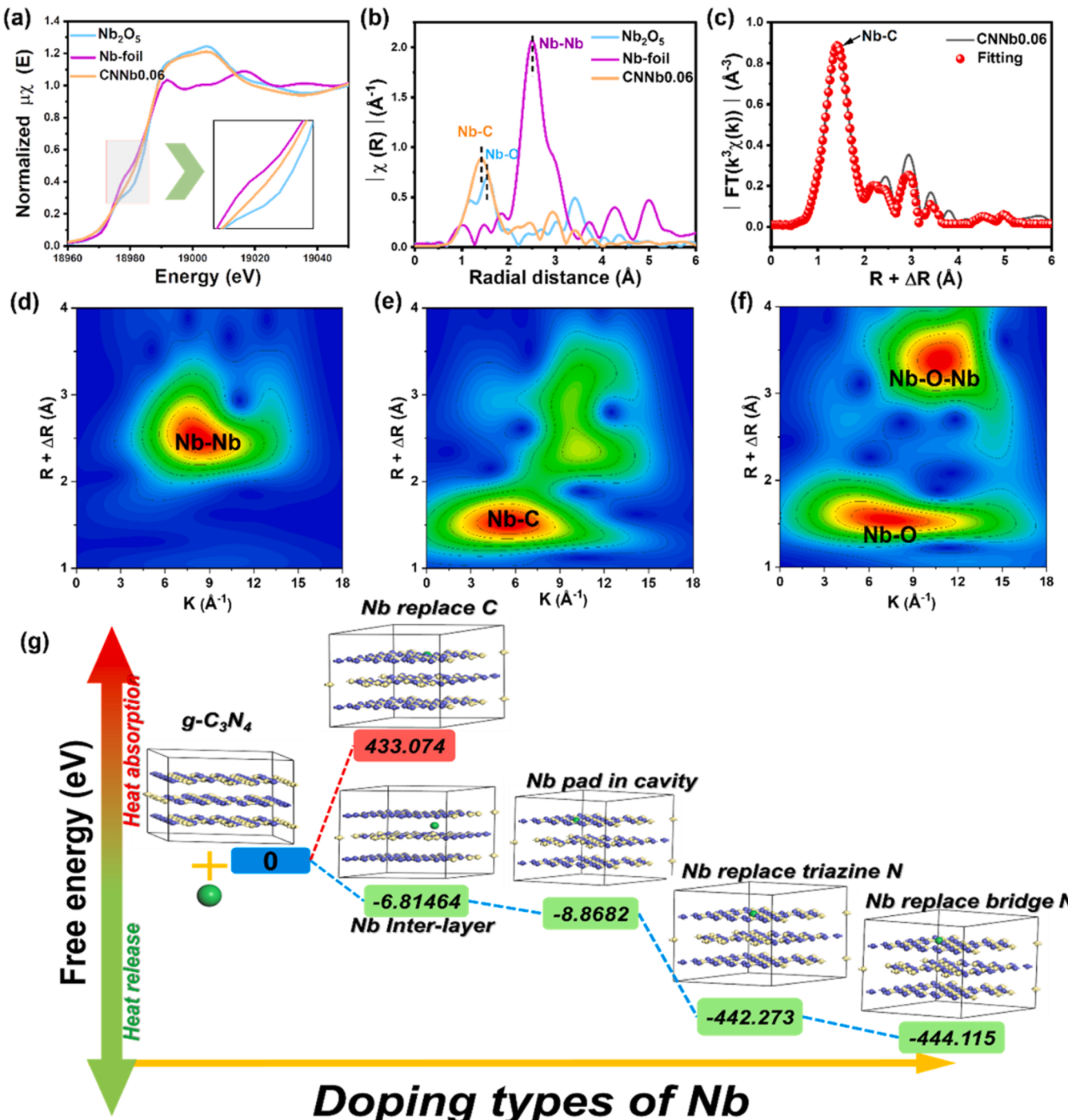


Fig. 3. Normalized Nb K-edge XANES spectra (a), FT $k^3(R)\chi(\text{Å}^{-1})$ vs Radial distance (Å) for Nb_2O_5 (blue), Nb-foil (magenta), and CNNb0.06 (orange). The diagram illustrates the free energy (eV) of various modes of single-atom Nb in DFT calculation. The vertical axis ranges from 0 (top) to -444.115 (bottom). The diagram shows energy levels for different modes: 0 (Nb in cavity), 433.074 (Nb replace C), -6.81464 (Nb Inter-layer), -8.8682 (Nb replace triazine N), -442.273 (Nb replace bridge N), and -444.115 (Nb in cavity). A legend indicates 'Heat absorption' (red arrow) and 'Heat release' (green arrow).

curve fitting was carried out. The fitting results explained that the isolated Nb atoms are coordinated with three atoms. According to the triazine ring structure of g-C₃N₄, it is supposed that the Nb center may replace bridged nitrogen and coordinate with three carbon atoms [41, 42]. Additionally, the K-space (Fig. S4) shows that the oscillation peaks of CNNb0.06, Nb, and Nb₂O₅ do not coincide, which further indicates that Nb in the CNNb0.06 system exists as a single atom.

As shown in Fig. S5a, CNNb0.06 and g-C₃N₄ showed an obvious EPR signal at $g = 2.004$ because the sp^2 -carbon atoms in the p-conjugated aromatic rings generated similar unpaired electrons. Specifically, the loss of the N atom in the structure left extra electrons that were redistributed to adjacent C atoms to form additional unpaired electrons [43]. After Nb anchoring, the amplitude of the CNNb0.06 curve was higher than that of the g-C₃N₄ curve, suggesting that massive defects were generated in the CNNb0.06. Similar results were reflected in the XPS data. The XPS analysis shows that the C/N value of the g-C₃N₄ is higher than CNNb0.06, and the peak areas ratio of C=N=C and N=C-N of CNNb0.06 are decreased compared to g-C₃N₄, indicating that the N defects mainly occurs at the bridged nitrogen site (Table S3). Although XPS data could not be very accurate, its trend is consistent with the results of EPR, which can be used as corroboration of EPR data. The increase in the value of C/N and decreased peak areas also indicate that the defects generated should belong to N vacancy. CHN elemental analysis further validates this result. As shown in Table S4, with the increasing of Nb anchored quantity, the percentage content of N element decreased most obviously. And this result was further determined by the intensity of EPR signal of the CNNbx samples in Fig. S5b.

Meanwhile, an amplitude with the $g = 1.865$ appeared in the EPR spectrum of CNNb0.06, corresponding to the signal of the Nb⁴⁺ with unpair electron. Considering the stability of Nb⁵⁺ higher than Nb⁴⁺, Nb⁵⁺ and C serve as electron acceptors and donors in Nb-C, respectively. This signal further explained the formation state of the Nb anchored on g-C₃N₄. A multitude of references dealing with possible forms of single-atom in g-C₃N₄ could be found, including intercalation in the interlayer of g-C₃N₄, replacement of N or C atoms, and filling in the cavity of g-C₃N₄ [17,44,45]. To further reveal the anchored style of Nb in the CNNb system, DFT calculations were used to investigate the required energy for various anchoring sites. The calculation results are summarized in Fig. 3g. Nb required the energy of 433.0742 eV to replace C atoms, implying absorption of great amounts of heat from outside. Hence, the replacement of C with Nb was challenging to achieve. The four anchoring methods, including interlayer intercalation, cavity padding, replacement of the bridging N, and triazine N, required approximately -6.81464 eV, -8.8682 eV, -444.155 eV, and -442.273 eV of energy, respectively. Here, negative energy meant an exothermic process, indicating the feasibility of all anchoring methods and replacement of the bridging N as the main anchoring method of Nb. However, the other three anchoring methods, including interlayer intercalation, cavity padding, and replacement of triazine N, were all energy-releasing processes, indicating the existence of a few remaining Nb atoms [45]. Compared with these results, the peak position of interlayer intercalation and cavity padding was not shifting with the Nb anchoring. The result suggested that Nb was mainly anchored on the N sites of g-C₃N₄, and the Nb-C bonds can be formed, it was consistent with the result of EPR and synchrotron radiation, and the anchoring mode is shown in Fig. S6. According to the above EXAFS fitting, the coordination number of Nb is 3, so Fig. S6b is most consistent with the structure of CNNb. The wavelet transform (WT) spectra in Fig. 3d-f reflected the distance of coordination atoms and distinguished the types of coordination atoms. The k value corresponding to the contour center of CNNb0.06 was also less than for the Nb foil and Nb₂O₅, further confirming that the isolated Nb elements tend to be atomically dispersed on the catalytic support and bond with C atoms in CNNb0.06 [23,40]. As for the formation reason of single atom Nb in CNNb0.06, on the one hand, the reducibility melamine can reduce the Nb element to a single atom [46]. On the other hand, in thermal polymerization, the formation of N vacancies in the

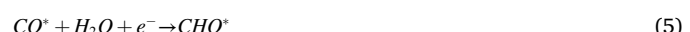
material could anchor Nb atoms and promote the formation of Nb-C bonds [47]. Combining the above factors led to the successful formation of single atom Nb.

It is well known that the high specific surface area can enhance the adsorption of pollutants on the surface of semiconductors, raising the number of active sites of systems. Thus, the specific surface areas of g-C₃N₄ and CNNb0.06 systems were compared by N₂ adsorption and desorption investigations (Fig. S7a), and the adsorption and desorption capacity of the CNNb0.06 system was higher than that of pristine g-C₃N₄, suggesting that anchoring with single atom Nb can greatly increase the specific surface areas of systems. The isotherms showed type-IV adsorption [47,48], with the specific surface area (S_{BET}) of CNNb0.06 estimated to be 15.36 m² g⁻¹. This value was 3.5-fold higher than in the case of pure g-C₃N₄ (4.41 m² g⁻¹). As shown in Fig. S7b, the pore diameter and pore volume of the CNNb0.06 system were also larger than those of g-C₃N₄. Hence, Nb anchoring increased the surface area of the semiconductors, enhancing the adsorption of pollutants on the surface of catalysts. This phenomenon is consistent with the results of the XPS-O1s spectra (Fig. 2f).

3.2. Photocatalytic performance and active species capture testing

The photocatalytic reduction activities of the as-prepared samples were evaluated through CO₂ reduction using a 300 W Xe lamp ($\lambda \geq 420$ nm). Fig. 4a and b show the time-dependent production yields of CO and CH₄ as functions of irradiation time. The g-C₃N₄ shows a relatively low activity compared with the other four samples. As shown in Fig. S8a and b, the evolutions of CO and CH₄ increased linearly with reaction time, indicating good stability in the CO₂ conversion process. The highest CO evolution of 221.2 μmol g⁻¹ was achieved using CNNb0.06 after 2 h, which was 3.3 times higher than g-C₃N₄. On the other hand, the CH₄ evolution of CNNb0.06 was 5.3 times higher than g-C₃N₄, indicating that the reductive ability of CNNb0.06 was much higher than that of g-C₃N₄. Moreover, the adsorption activity of g-C₃N₄ and CNNb0.06 for CO₂ was further analyzed by CO₂-TPD. As shown in Fig. S9, the peak intensities of CNNb0.06 were higher than that of g-C₃N₄, indicating that CNNb0.06 has better adsorption and desorption activity for CO₂. Most noticeably, the absorption peak at 600 °C was much higher than that of g-C₃N₄, meaning that the CNNb0.06 has strong adsorption-desorption stability and activity for CO₂. Hence, the CNNb0.06 was easier to reduce more CO₂ than g-C₃N₄ and has a more stable active center for CO₂ reduction. Moreover, the durability of CNNb0.06 for CO₂ reduction was further verified by five cycles. As shown in Fig. S8c, the yield of CO and CH₄ did not decrease significantly after five cycles, indicating that CNNb0.06 has the ability to maintain stability in the process of photocatalytic CO₂ reduction.

To explore the mechanisms of photocatalytic CO₂ conversion, the CO₂ reduction process from 5 to 60 min was tested by in-situ FTIR. As exhibited in Fig. 4d, the in-situ FTIR spectra mainly consisted of eight peaks at 1085 cm⁻¹ (CHO*), 1130 cm⁻¹ (CH₃O*), 1260 cm⁻¹ (CO₃²⁻), 1340 cm⁻¹ (HCO₃⁻), 1490 cm⁻¹ (COOH*), 1690 cm⁻¹ (COOH*), 1719 cm⁻¹ (C=O), and 2360 cm⁻¹ (adsorbed CO₂), respectively [49–51]. Thus, the possible CO₂ reduction mechanism of CNNb0.06 as the following (2–7):



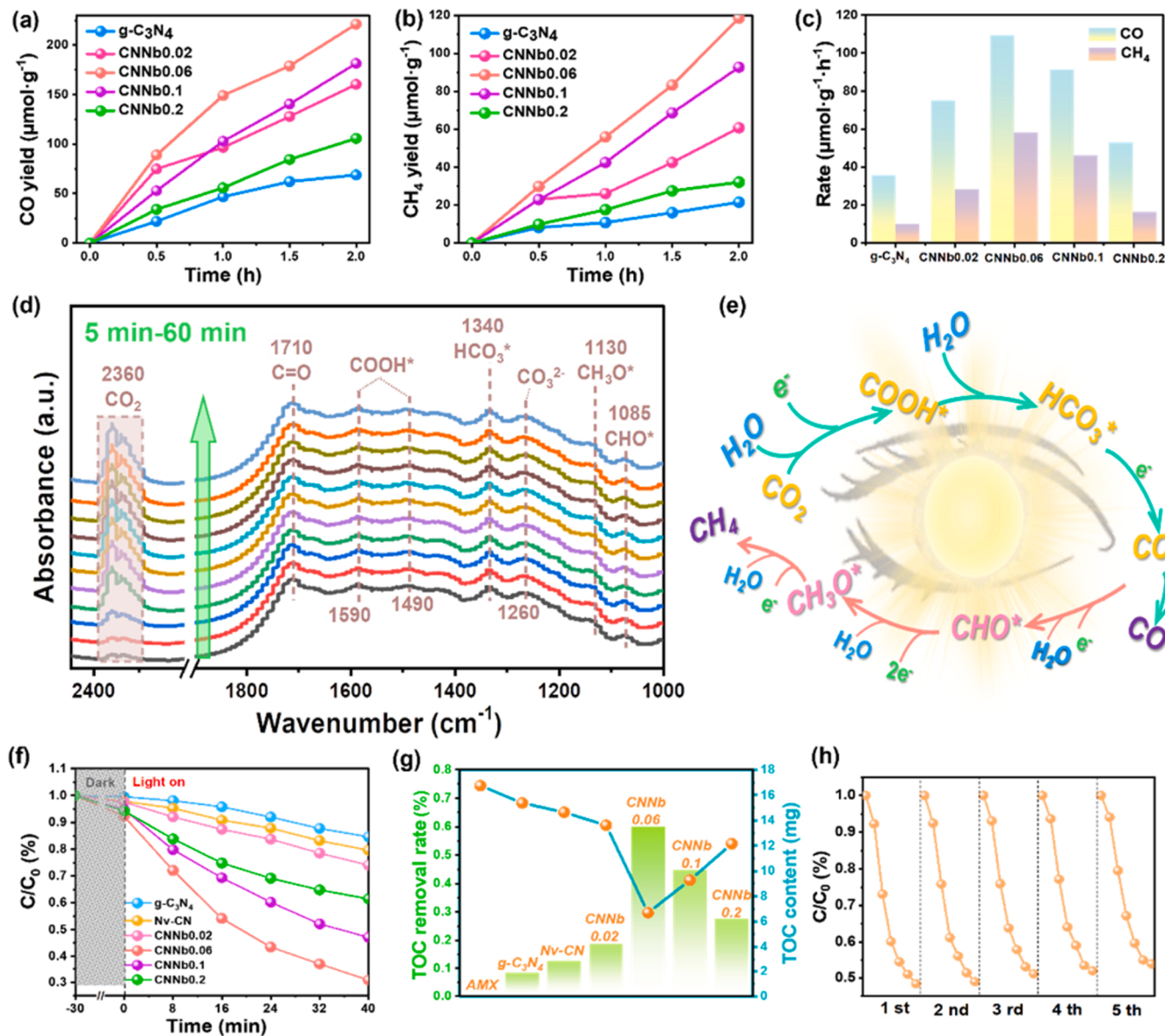


Fig. 4. The evolution-time curves of CO (a) and CH_4 (b); evolution rates (c) of CO and CH_4 for as-prepared samples; the in-situ FTIR spectroscopy (d) of CO_2 reduction by CNNb0.06; conversion process (e) of CO_2 by CNNb0.06; degradation efficiency of AMX by samples (f); TOC removal rate and content (g) by as-prepared samples under visible light irradiation; 5th cycle experiment on degradation of AMX by CNNb0.06 (h).

The conversion process of CNNb0.06 to CO_2 was proposed in Fig. 4e. Under the irradiation of visible light, CO_2 needed to capture two electrons to generate CO and six electrons to generate CH_4 . The selectivity of CO_2 reduction reaction for CNNbx catalysts and $\text{g-C}_3\text{N}_4$ were further compared in Fig. S10 and Table S5. The CNNb0.06 shows the highest CH_4 selectivity among these catalysts. These results showed that the number of free electrons produced by CNNb0.06 was much higher than that of $\text{g-C}_3\text{N}_4$. As shown in Figs. 4c, S8a and b, the CO and CH_4 evolution yields and rates of CNNb0.1 and CNNb0.2 decreased compared to CNNb0.06 with the increased Nb content. This could indicate that the anchoring amount of Nb plays a critical role in the photocatalytic reduction. Excess Nb amount was disadvantageous for the reduction of CO_2 . This result might be because excessive single-atom Nb and N vacancies accelerated the charge recombination.

Furthermore, the photocatalytic activities were evaluated using AMX as the target pollutant. As shown in Fig. S11, the large gap between the HOMO and LUMO orbitals indicated an extremely photostable molecular structure of AMX. Thus, the photolytic decomposition of AMX was almost negligible in the absence of a photocatalyst. As shown in Fig. 4f

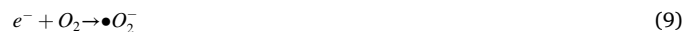
and g, the photocatalytic removal rates of pollutants were low in the presence of pure $\text{g-C}_3\text{N}_4$. Furthermore, the photocatalytic activities of CNNb catalyst composites highly depended on amounts of incorporated Nb. The AMX removal efficiency of CNNb0.06 was enhanced from 15.3% to 69.1% compared to pure $\text{g-C}_3\text{N}_4$. The kinetics of AMX removal by the as-prepared samples were defined as a first-order reaction (Fig. S12), and CNNb0.06 demonstrated the highest rate constant of 0.0269 min^{-1} . The mineralization degree using the as-prepared photocatalysts for degrading AMX was evaluated by TOC analysis (Fig. 4g). It was found that the CNNb0.06 had the highest efficiency rate of AMX mineralization, which was 6 times higher than that of pure $\text{g-C}_3\text{N}_4$ in 30 min. Furthermore, the photocatalytic stability of the CNNb0.06 was tested by five degradation cycles. There was no significant decrease in the degradation ability of AMX by CNNb0.06 after five cycles (Fig. 4h), indicating that the active center of oxidation ability was relatively stable in CNNb0.06.

Combining the CO_2 conversion of each catalyst and the degradation process of AMX, it was proved that CNNb0.06 presented the highest photocatalytic redox ability. With the continuous increase of the

anchored amount of Nb, both the photocatalytic reduction and oxidation activities exhibited a decreasing trend. The result may be attributed to the excess Nb, which could agglomerate, covering the active sites of catalysts and blocking the charge transfer. Compared to previously reported results, the performance of photocatalytic removal of AMX over CNNb0.06 was significantly enhanced (Table S6). The as-enhanced photocatalytic performance may be attributed to the synergistic effect of single-atom Nb and N defects in CNNb0.06. Both aspects will be discussed below.

Active species trapping experiments with different scavengers were performed to the various roles of active species for degrading AMX over $\text{g-C}_3\text{N}_4$ and CNNb0.06. To elucidate this aspect, triethanolamine (TEOA), potassium dichromate ($\text{K}_2\text{Cr}_2\text{O}_7$), p-benzoquinone (PBQ), and isopropanol (IPA) were applied as masking agents for h^+ , e^- , $\bullet\text{O}_2^-$, and $\bullet\text{OH}$, respectively. Compared to $\text{g-C}_3\text{N}_4$, the addition of KI and PBQ significantly restrained the removal of AMX in CNNb0.06, identifying the $\bullet\text{O}_2^-$ as the main active specie for AMX removal in CNNb0.06 (Fig. 5a and b). Comparing the performance of the two catalysts with the addition of IPA was found that the degradation ability of $\text{g-C}_3\text{N}_4$ was

enhanced. In contrast, the degradation process of CNNb0.06 was inhibited, indicating that more $\bullet\text{OH}$ was produced in CNNb0.06 than in $\text{g-C}_3\text{N}_4$. To sum up, the possible mechanism AMX oxidation reactions of CNNb0.06 under visible light irradiations are shown in the following (8–13):



Additionally, the formation of some intermediates before the complete mineralization of AMX to CO_2 and H_2O was analyzed by HPLC-MS

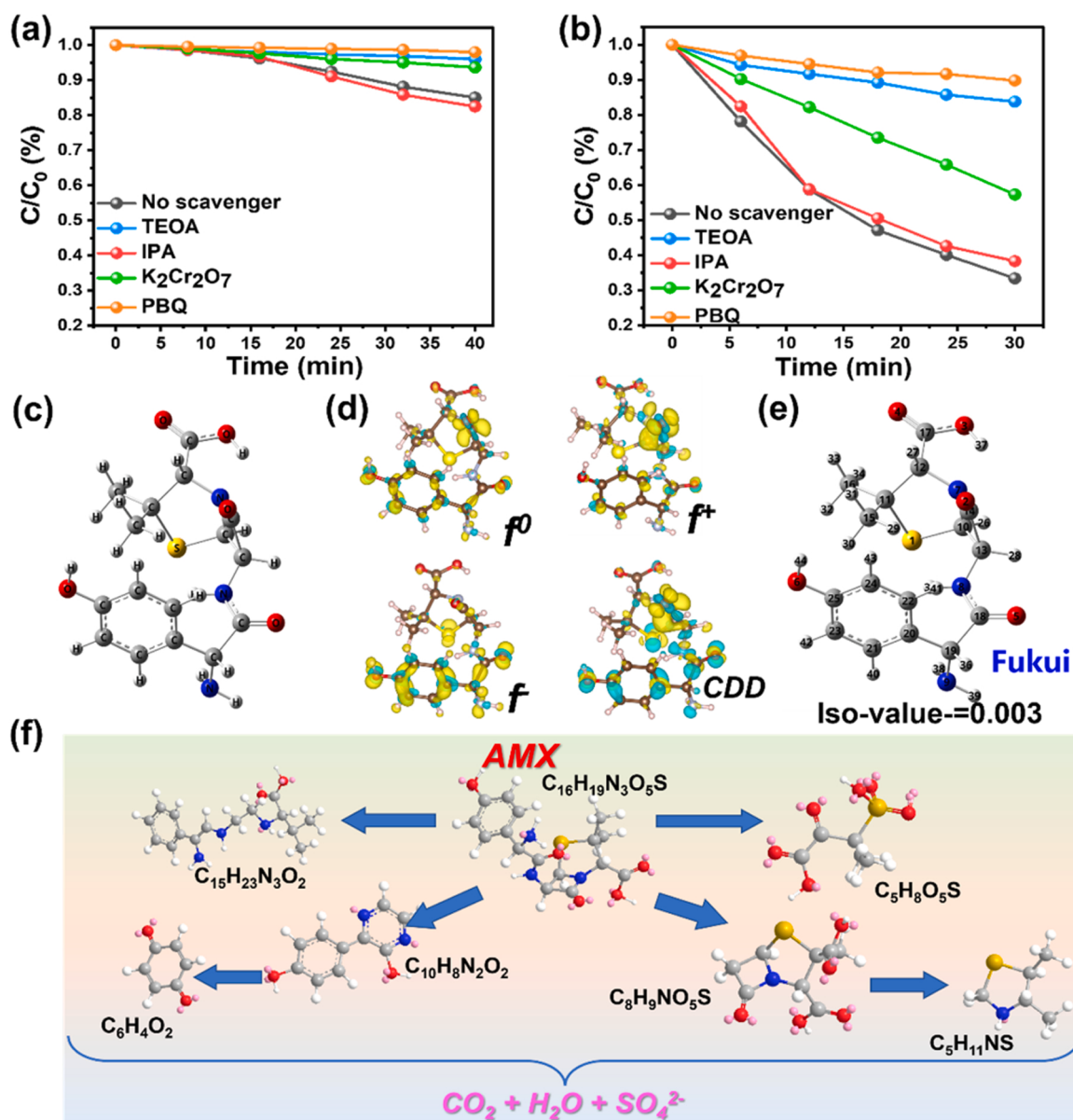


Fig. 5. AMX removal with different scavengers in $\text{g-C}_3\text{N}_4$ (a) and CNNb0.06 (b) under visible light irradiation; the iso-surface of Fukui index (c ~ e) color code: C (gray), O (red), N (blue), S (yellow) and H (white); the main pathways of AMX removal by CNNb0.06 (f).

(Fig. S13a–d). Meanwhile, the Fukui index described the radical attack of the atoms on the AMX molecule as determined by DFT (Fig. 5c–e and Table S7). The O2, O5, O6, C14, C20, C22, C23, C24, C25, and S1 atoms exhibited higher f^0 values than other atoms, indicating that these atoms would be vulnerable to attack by electrophile or reactive species. Based on the theoretical calculations and experimental results, we proposed three possible AMX removal pathways, and the main intermediate products are presented in Figs. 5f and S14. (The experimental details of the removal pathways of AMX were illustrated in Text S7 of Supporting Information).

It was well known that pristine g-C₃N₄ can hardly produce •OH and •O₂⁻ [46,52,53]. Interestingly, the above experiments ended the Nb anchoring with a special performance for g-C₃N₄. The reasons for CNNb0.06, which can simultaneously produce two reactive oxygen species (•OH and •O₂⁻), and the excellent photocatalytic activity will be discussed in the following section.

3.3. Enhanced photocatalytic performance mechanism

The electron transfer ability is one of the important parameters for judging the photocatalytic activity of semiconductors. The photoelectric properties of the samples were further evaluated by electrochemical measurements. The Nyquist plots revealed semicircles in high-frequency regions corresponding to electron transfer-limited processes. The

diameter of the semicircle in CNNb0.06 significantly declined more than that in the g-C₃N₄ Nv-CN plots (Fig. 6a). Meanwhile, TPR was used to investigate the charge migration capacity under visible light for photocatalysts. As shown in Fig. 6b, the transient photocurrents of CNNb0.06 were more intense than those of pure g-C₃N₄ and Nv-CN, meaning that a lower charge transfer resistance on the sample surface involves high transfer efficiency of photocarriers. The resistance values of the corresponding resistor were obtained by fitting the EIS curves, and the data are listed in Table S8. The equivalent circuit diagram is shown in Fig. 6a. The electrolyte, working electrode, and surface polarization resistance are defined as R₁, R₂, and R₃, respectively, and the R₃ of g-C₃N₄ and Nv-CN both higher than that of CNNb0.06. According to previous results [46,53,54], the generated N defects could promote the conversion of excitons to photogenerated carriers.

Combined with the above characterizations, the decrease of R₃ is attributed to the fact that N defects produced a large number of photogenerated carriers, which increased the photocurrent on the surface of the sample and decreased the resistance value accordingly. Furthermore, the R₃ of CNNb0.06 less than that of Nv-CN may be attributed to the excellent conductivity of polarized Nb-C bonds that would transfer charges produced at the conduction band composed of Cp_z. Thus, we gathered that the impedance decrease was attributed to the synergistic effect of the Nb-C bond and N defect in CNNb0.06. DFT calculations were also used to explain the results of electrochemical measurements.

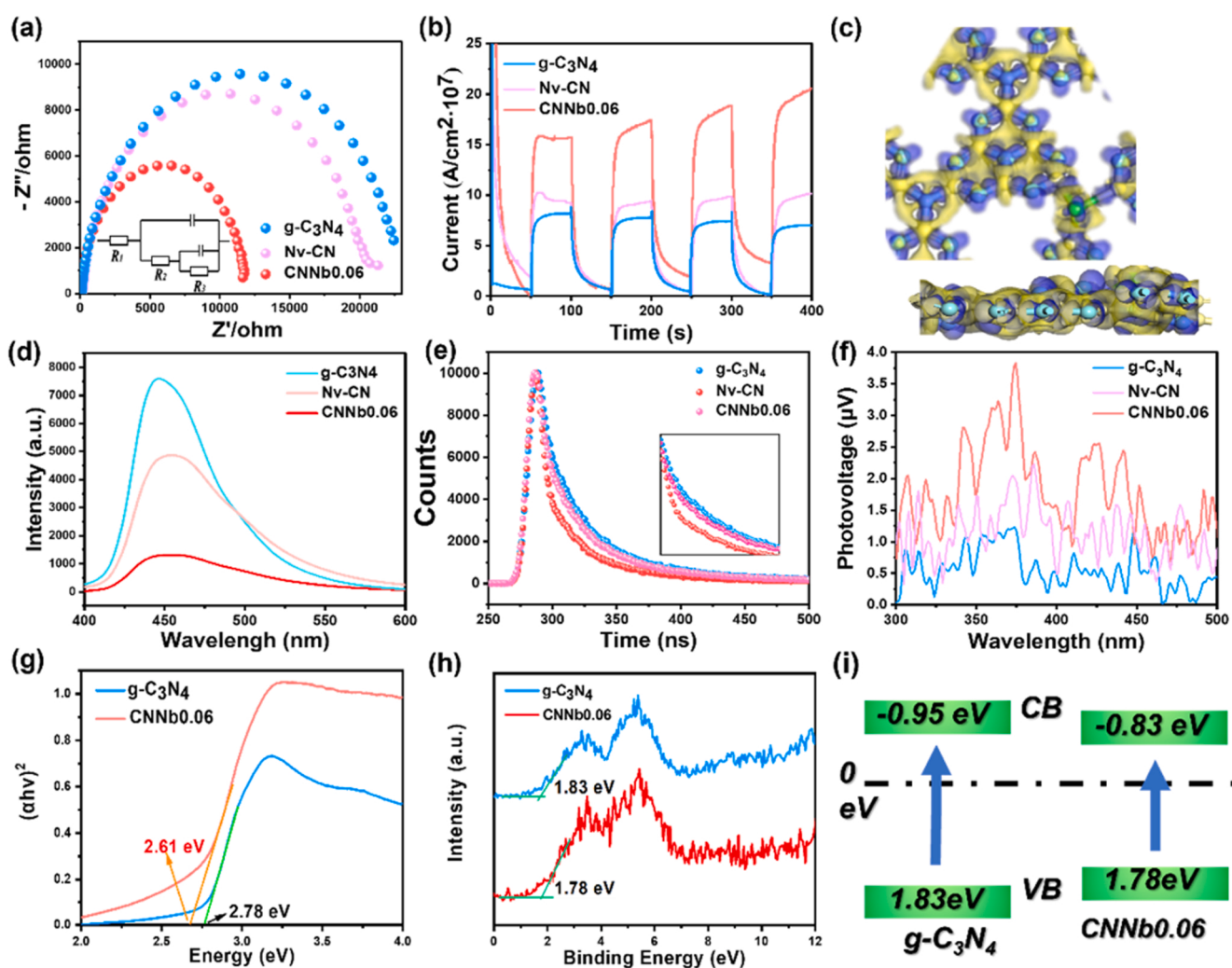


Fig. 6. Nyquist plots (a) and the equivalent circuits; transient photocurrent spectra (b); differential charge density of CNNb structure (c); PL spectra (d); the Tr-PL spectra (e); SPV spectra (f); the transformed Kubelka-Munk function of the g-C₃N₄ and CNNb0.06 (g); XPS valence spectra (h) of g-C₃N₄ and CNNb0.06. The band structure (i).

Fig. S15a and b showed the theoretical calculations of the electron cloud density of systems. The electron densities of various systems looked almost the same. The differential charge of g-C₃N₄ and CNNb was displayed in **Figs. S15c and 6c**, respectively. Similarly, there is no obvious change in the charge density difference with the anchoring of Nb, meaning that the existence of Nb-C did not increase the number of electrons in the systems but mainly enhanced the conduction in the CNNb0.06 system. This led to an improved photocatalytic performance of the CNNb system.

Photoluminescence (PL) was used to examine the separation efficiency of photogenerated electrons and holes (**Fig. 6d**). Pure g-C₃N₄ showed a strong emission peak at about 452 nm due to the high recombination rate of photogenerated carriers. The fluorescence intensity of sample CNNb0.06 was much lower than that of g-C₃N₄, meaning that Nb-anchoring could inhibit the recombination of photogenerated carriers. The ns-level time-resolved fluorescence decay spectra were also shown in **Fig. 6e**. The fluorescence lifetime of Nv-CN is only a little lower than that of pure g-C₃N₄, explaining that the formation of N vacancies can not significantly accelerate the charge transfer, but may only play a role in transforming excitons into carriers. Moreover, the CNNb0.06 had a lowest fluorescence lifetime among three catalysts, indicating that the Nb-anchored system could efficiently accelerate electron conduction, promoting the separation of photogenerated carriers.

In addition, the charge separation extent, charge separation, and surface-potential barrier of the excited state produced by absorption were further revealed from the surface photovoltage (SPV) spectroscopy. It was observed that the SPV generated by CNNb0.06 with an enhancement degree of over 3-fold compared to g-C₃N₄ in the range of 300–500 nm (**Fig. 6f**), revealing the more accelerated photocarrier separation efficiency. This phenomenon was consistent with the above electrochemical tests and PL results. Therefore, it was confirmed the excellent CO₂ reduction ability and high CH₄ yield of CNNb0.06.

Photogenerated carriers' excitation in photocatalysis mainly depends on the absorption capacity of light of the photocatalysts. Therefore, the optical performances of semiconductors could significantly affect photocatalytic activities. The UV-vis diffuse reflectance spectra were measured to evaluate the band gaps of the samples. As displayed in **Fig. S16a**, the UV-vis absorption spectra of CNNbx bathochromic shifted when compared to g-C₃N₄, showing that anchoring of Nb broadened the light absorption region of g-C₃N₄. In **Figs. S16b** and **6g**, the energy band gaps of samples were calculated by **Eq. (14)**:

$$(ahv)^2 = A(hv - E_g) \quad (14)$$

The energy band gaps of g-C₃N₄ and CNNb0.06 were estimated to be 2.76 and 2.67 eV, respectively. On the other hand, normalized of the UV-vis/DRS spectra (**Fig. S16c**) exhibited that CNNb catalysts exhibited significantly enhanced photocatalytic activities compared to pure g-C₃N₄. Thus, the existence of Nb narrowed the band gaps of CNNb0.06 and further indicated the anchoring of Nb enhanced the light absorption capacity of the catalyst and improved the energy conversion efficiency.

On the other hand, DFT calculations could explain the band gaps of as-prepared samples. For example, Nb replaced bridged nitrogen (**Fig. S17b**), revealing that Nb anchoring formed impurity bands in the band gap and narrowed it in comparison to g-C₃N₄ (**Fig. S17a**). Meanwhile, the energy density of Nb anchored on g-C₃N₄ was much higher than that of pure g-C₃N₄. In general, the band gap of semiconductor materials is about one to three electron volts. An energy gap of zero or very narrow would correspond to a good-quality conductive material. As shown in **Fig. S17b**, the energy gap was narrower than 0.5 eV in the CNNb system, illustrating Nb atoms' efficient ability to conduct electrons. Although the calculation of the energy gap was not very accurate, its trend was consistent with the UV-vis diffuse results. However, narrowing the band gap would tend to the faster recombination of photogenerated carriers [9,55,56]. This was contrary to the results

investigating the photocatalytic activity and SPV. It would be because the excellent electron transport ability of the Nb-C bonds could effectively transfer charge and greatly restrain the recombination of carriers. To identify this inference, the density of states (DOS) analysis of g-C₃N₄ and CNNb0.06 were calculated by DFT. Referring to DOS analysis, the Nb anchoring greatly increased the electron energy, confirming the strong separation ability of photogenerated carriers in CNNb. Meanwhile, the anchoring of the Nb atom leads to the generation of a large number of N defects and destroys the *sp*²-hybridization of C, which lead to the increase of unpair electrons in p orbitals. Furthermore, compared to g-C₃N₄, the Fermi level of the CNNb system was between two sharp peaks, and its value was not zero. This demonstrated that the photocatalyst had a semi-metallic characteristic after Nb anchoring, confirming that the Nb-C enhanced the electrical conductivity in CNNb [57]. As a theoretical calculation method, the energy gap data and DOS may not be accurate. However, this result can be used as a preliminary estimation of the N-vacancy that cooperates with the Nb-C bond to enhance the electrical conductivity of CNNb0.06. This further confirms the results of electrochemical impedance spectroscopy (EIS) and transient photocurrent responses (TPR) analysis. As shown in **Fig. 6h**, the valence band (VB) potentials measured by VB-XPS were 1.83 eV and 1.78 eV, respectively. The conduction band (CB) potentials were described by **Eq. (15)**:

$$E_g = E_{VB} - E_{CB} \quad (15)$$

where E_g represents the band gap energy of the sample. E_{VB} and E_g are the valence band energy and conduction band energy, respectively. The CB potentials of g-C₃N₄ and CNNb0.06 were calculated as –0.93 eV and –0.89 eV, respectively. It is worth noting that the CB potential of CNNb0.06 was lower than that of g-C₃N₄. Theoretically, the reduction effect of CNNb0.06 on CO₂ was weaker than that of g-C₃N₄. However, the actual evolution of CO and CH₄ by CNNb0.06 is much higher than that of g-C₃N₄. In order to find out the cause of this phenomenon, the DFT calculation of differential charge was carried out for the structures of CNNb-CO₂ and g-C₃N₄-CO₂. As exhibited in **Figs. 7a** and **S15c**, the charge density distribution of g-C₃N₄ had almost no change before and after the existence of CO₂. Nevertheless, the charge distribution around Nb has changed significantly when the CO₂ was introduced in CNNb. The **Fig. 7a** showed that the yellow electron clouds became more centered on Nb in the CNNb-CO₂ system. The increasement of yellow electron clouds meant the acquire electronic ability and the reducibility were enhanced for the reduction of CO₂. This calculation of charge difference density was consistent with the experiment result of CO₂ reduction. This phenomenon indicates that the charge near Nb-C is unstable, and when there is an electron acceptor in the system, more electrons will be spilled over through the conduction Nb-C. To further understand the high charge transfer efficiency, the HOMO and LUMO of the CNNb was calculated to investigate the charge distribution (**Fig. 7b**). Various reports were in identification that the LUMO and HOMO have nearly equal energy in the g-C₃N₄ unit which composed of Npz and Cpz orbitals, and the electron evenly dispersed within the triazine ring structure [44,47]. Surprisingly, the HOMA and LUMO orbitals of the Nb anchored on g-C₃N₄ were clustered on Nb-C bonds, and the value of ΔE is so small (< 1 eV). This phenomenon was meaning that Nb-C had a sensitive charge transfer ability. According to the charge arrangement of Nb, the +5 valence Nb is the most stable. However, the above XPS test results show that the valence distribution of Nb is mainly +5 and +4, and the relative content of Nb⁴⁺ in CNNb0.06 is the highest among all CNNbx catalysts (**Table S1**). The existence of Nb⁴⁺ showed that the Nb is the electron absorption site between Nb-C, which can also be proved by EPR (there was a signal of lone pair electrons trapped by Nb ions), which indicates that the formation of polar Nb-C can promote electron migration. After illumination, the photogenerated electrons produced on LUMO migrate to the valence band along C-Nb and enrich near Nb, making the Nb-C bond become the redox active center of the system.

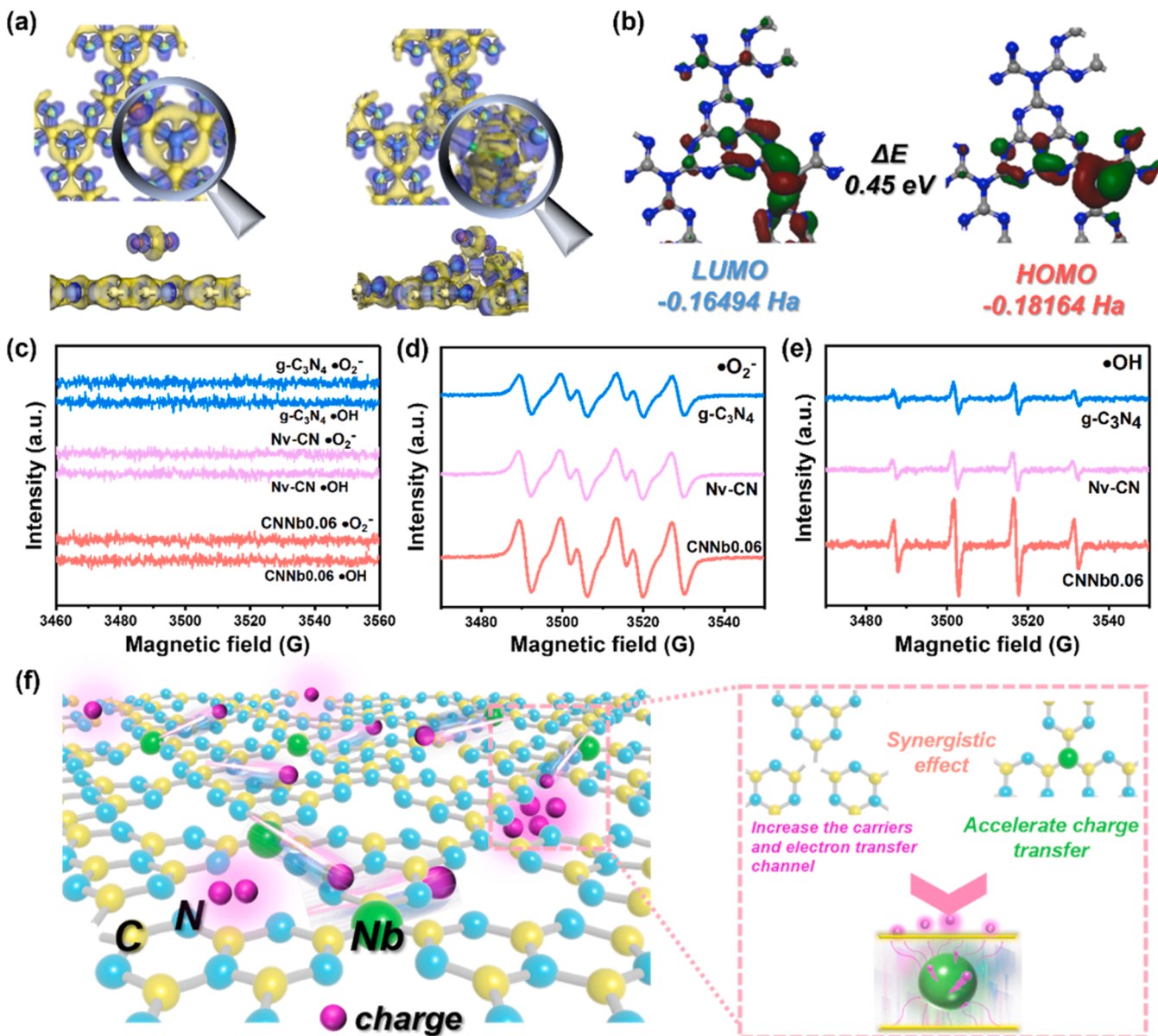


Fig. 7. The differential charge density (a) of CO₂-C₃N₄ and CO₂-CNNb. The frontier molecular orbital (b) of CNNb. The production of •O₂⁻ and •OH was detected with DMPO spin-trapping ESR technique for g-C₃N₄, Nv-CN and CNNb0.06 in dark (c) and under visible light irradiation (d and e). Charge conduction mechanism (f) of single-atom Nb anchored on g-C₃N₄.

Additionally, the DFT calculation of the charge difference density of the CNNb systems with different N vacancy (Nv-CNNb) were carried out (Fig. S18) to determine the effect of the existence of N on the charge localization of the system. Compared with Fig. S18a and b, it is found that the N vacancy only accumulates part of the charge in the presence of the electron acceptor. By comparing Fig. S18 with Fig. 7a, we can see that the existence of N vacancy has no significant effect on the gain and loss ability of charge around Nb and the reduction ability of CO₂. The photocatalytic performance of CNNb0.1 and CNNb0.2 were weaker than that of CNNb0.06, mainly due to the increase of Nb anchoring in the synthesis process, which led to the increase of Nb⁵⁺ in the system, while the reducibility of melamine was difficult to reduce too much Nb⁵⁺ to Nb⁴⁺. Therefore, the photocatalytic performance has a negligible change with the increasing amount of Nb and the N vacancies. Combining with the above characterization of the photoelectric properties, the existence of N vacancy only promotes the conversion of more excitons to photogenerated carriers. And the main factors that promote charge transfer and localization to enhance the photocatalytic activity of

the catalysts are the conductivity of Nb-C and the change of valence state of Nb.

As shown in Fig. 6i, the potential of VB and CB in CNNb0.06 were both weaker than g-C₃N₄. The potential of VB and CB would be the principal factor generating reactive oxygen species since •O₂⁻ and •OH was produced by the redox reaction of photocarriers. The 5,5-dimethyl-1-pyrroline N-oxide (DMPO) spin-trapping ESR technique was employed to detect •O₂⁻ and •OH in g-C₃N₄, Nv-CN and CNNb0.06 for comparing the content of active oxygen species. As shown in Fig. 7c, none of the three catalysts could produce •O₂⁻ and •OH in dark condition. Furthermore, Fig. 7d and e exhibited that the signals of •O₂⁻ and •OH of CNNb0.06 were much higher than those of g-C₃N₄ and Nv-CN under visible light irradiation. The active oxygen species signal of Nv-CN was only slightly stronger than that of g-C₃N₄, indicating that although vacancy defects increased the number of charges, it could not effectively inhibit the recombination of photogenerated carriers, consistent with the results of optoelectronic performance tests. Therefore, it could be affirmed that the carrier recombination in CNNb0.06 was dramatically

suppressed, which explained the reason of the highest CH₄ yield of CNNb0.06 (CO₂ + 6H⁺ + 6e⁻ → CH₄ + H₂O). This was consistent with frontline orbit results of CNNb, the Nb-C was the redox active center in CNNb0.06. However, it was already found that the potentials of VB holes from CNNb0.06 (1.78 eV) and g-C₃N₄ (1.83 eV) were both lower than that of OH⁻/•OH potential (1.99 eV) and cannot directly oxidize OH⁻ into •OH (Fig. 6i), but both photocatalysts may produce •O₂⁻ (CB < -0.33 eV). Based on previous reports, •OH may be generated through either single-electron reduction (•O₂⁻ → H₂O₂ → •OH) [58,59]. It is worth noting that the potential energy of VB and CB of CNNb0.06 was lower than that of g-C₃N₄, and the ability of CNNb0.06 to produce reactive oxygen species (•O₂⁻ and •OH) would be weaker than that of g-C₃N₄ in theory. Remarkably, the concentration of reactive oxygen species in CNNb0.06 was much higher than that in g-C₃N₄ and Nv-CN, which meant that the anchoring of single-atom Nb greatly optimized the redox ability of g-C₃N₄. From the above DFT calculations and the analysis of photoelectronic properties, it was shown that the conductive ability of CNNb0.06 was stronger than that of g-C₃N₄. Therefore, the increase of •O₂⁻ was mainly attributed to the enhancement of electron transfer ability in CNNb0.06 (O₂ + e⁻ → •O₂⁻), and the •OH content increased in CNNb0.06 might be produced by single electron reduction. In turn, the tests of H₂O₂ production in both systems were performed to verify this conjecture further. After illumination for 30 min, the amount of H₂O₂ produced by CNNb0.06 was higher than that of g-C₃N₄, indicating that the concentration of •O₂⁻ in CNNb0.06 was higher than that in g-C₃N₄, consistent with the test results of ESR. Furthermore, the H₂O₂ concentration-time variation trend of g-C₃N₄ and CNNb0.06 were analyzed to judge their ability to produce hydroxyl radicals. As shown in Fig. S19a and b, the signal intensity of H₂O₂ generation in g-C₃N₄ continuously grew, ruling out the decomposition of H₂O₂ in the g-C₃N₄ system. For CNNb0.06, the signal intensity of the generated H₂O₂ started to fluctuate after 40 min (Fig. S19c and d), meaning a significant decomposition of H₂O₂ in the CNNb0.06 system. The generation of •OH was further investigated and compared for both systems (Fig. S19e and f). The production of •OH in CNNb0.06 was conspicuously higher than in g-C₃N₄ under visible light irradiation, consistent with the results of ESR (Fig. 7e). Therefore, the anchoring of Nb facilitated the •OH formation in the g-C₃N₄. With the formation of N defects and Nb-C with single atom Nb anchoring increased the charge density and the separation of photogenerated carriers and improved the ability of single-electron reduction (H₂O₂ + e⁻ → •OH + OH⁻), decomposing H₂O₂ to generate •OH. Meanwhile, the increase of electron density and the enhancement of adsorption strengthened the ability of the CNNb0.06 system to produce •O₂⁻. The synergistic effect of various factors made the single-atom Nb-anchored g-C₃N₄ to show outstanding reactive oxygen species formation ability. The results declared that the Nb-C transferred the charge produced by N defects in a form similar to "high-speed rail", which efficiently suppressed the recombination of photogenerated carriers and intensified the redox semi-reaction by taking Nb-C bond as the active center (Fig. 7f).

4. Conclusions

In summary, a simple thermal polymerization method was used to prepare the single-atom Nb-anchored g-C₃N₄-based photocatalysts. The optimized CNNb0.06 showed an excellent photocatalytic redox efficiency for reducing CO₂ and oxidation of AMX under visible light irradiation. Based on a series of characterizations and DFT calculations, the anchoring of Nb in g-C₃N₄ narrowed the band gap. It enhanced the ability to absorb visible light, while the formation of Nb-C bonds accelerated the separation and transfer of photogenerated carriers to inhibit the recombination rate of photogenerated electron-hole pairs. Meanwhile, the incorporation of d orbitals and the generation of N defects led the changes in internal electronic structure, which were helpful to the increase of charge transfer channels. Thus, the enhanced photocatalytic performance of CNNb0.06 was mainly attributed to the

synergistic effect of Nb-C and N defects. This study sheds light on the basic reference for the design of transition metal single-atom modified catalysts with efficient photocatalytic redox ability.

CRediT authorship contribution statement

Jianmin Luo: Supervision, Writing – review & editing. **Haonan Han:** Data curation, Writing – original draft. **Xinglei Wang:** Data curation. **Xiuzhen Qiu:** Data curation. **Yinlong Lai:** Data curation. **Lei Wang:** Validation, Visualization. **Chuanyi Wang:** Supervision.

Declaration of Competing Interest

The authors declare that they have no known competing financial interests or personal relationships that could have appeared to influence the work reported in this paper.

Data availability

Data will be made available on request.

Acknowledgments

This work was partially supported by the Guangdong Basic and Applied Basic Research Foundation under Grant 2021A1515010060, 2021A1515010185 and 2021A1515010671, in part by Yili Normal University Scientific Research Project under Grant 2022YSZD007, in part by Guangdong Province Scientific Research Platform Project under Grant 2022ZDZX4046 and 2020KCXTD037, in part by the Guangdong Province Specialized Scientific Research Fund Projects, and in part by the Guangdong Province University Engineering Technology Center Projects under Grant 2021GCZX011, in part by the College Student Innovation and Entrepreneurship Project under Grant 202210576011, in part by High Level Talents Introduction Project of "Pearl River Talent Plan" in Guangdong Province (No. 2019CX01L308).

Appendix A. Supplementary material

Supplementary data associated with this article can be found in the online version at doi:10.1016/j.apcatb.2023.122495.

References

- [1] D. Kanakaraju, J. Kockler, C.A. Motti, B.D. Glass, M. Oelgemöller, Titanium dioxide/zeolite integrated photocatalytic adsorbents for the degradation of amoxicillin, *Appl. Catal. B Environ.*, 166–167 (2015) 45–55, <https://doi.org/10.1016/j.apcatb.2014.11.001>.
- [2] A. Mirzaei, Z. Chen, F. Haghigiat, L. Yerushalmi, Magnetic fluorinated mesoporous g-C₃N₄ for photocatalytic degradation of amoxicillin: transformation mechanism and toxicity assessment, *Appl. Catal. B Environ.* 242 (2019) 337–348, <https://doi.org/10.1016/j.apcatb.2018.10.009>.
- [3] Y. Wang, G. Zuo, J. Kong, Y. Guo, Z. Xian, Y. Dai, J. Wang, T. Gong, C. Sun, Q. Xian, Sheet-on-sheet TiO₂/Bi₂MoO₆ heterostructure for enhanced photocatalytic amoxicillin degradation, *J. Hazard. Mater.* 421 (2022), 126634, <https://doi.org/10.1016/j.jhazmat.2021.126634>.
- [4] S. Le, Y. Ma, D. He, X. Wang, Y. Guo, CdS/NH₄V₄O₁₀ S-scheme photocatalyst for sustainable photo-decomposition of amoxicillin, *Chem. Eng. J.* 426 (2021), 130354, <https://doi.org/10.1016/j.cej.2021.130354>.
- [5] M. Wang, L. Zhang, G. Zhang, T. Pang, X. Zhang, D. Cai, Z. Wu, In situ degradation of antibiotic residues in medical intravenous infusion bottles using high energy electron beam irradiation, *Sci. Rep.* 7 (2017) 39928, <https://doi.org/10.1038/srep39928>.
- [6] M. Moradi, F. Hasanzandian, A.A. Isari, F. Hayati, B. Kakavandi, S.R. Setayesh, CuO and ZnO co-anchored on g-C₃N₄ nanosheets as an affordable double Z-scheme nanocomposite for photocatalytic decontamination of amoxicillin, *Appl. Catal. B Environ.* 285 (2021), 119838, <https://doi.org/10.1016/j.apcatb.2020.119838>.
- [7] M. Dou, J. Wang, B. Gao, C. Xu, F. Yang, Photocatalytic difference of amoxicillin and cefotaxime under visible light by mesoporous g-C₃N₄: Mechanism, degradation pathway and DFT calculation, *Chem. Eng. J.* 383 (2020), 123134, <https://doi.org/10.1016/j.cej.2019.123134>.
- [8] Xa Dong, J. Li, Q. Xing, Y. Zhou, H. Huang, F. Dong, The activation of reactants and intermediates promotes the selective photocatalytic NO conversion on electron-

- localized Sr-intercalated g-C₃N₄, *Appl. Catal. B Environ.* 232 (2018) 69–76, <https://doi.org/10.1016/j.apcatb.2018.03.054>.
- [9] H. Han, X. Wang, Y. Qiao, Y. Lai, B. Liu, Y. Zhang, J. Luo, S. Toan, L. Wang, Construction of S-scheme heterojunction for enhanced photocatalytic conversion of NO over dual-defect CeO_{2-x}/g-C₃N_{4-x}, *J. Alloy. Compd.* 933 (2023), 167819, <https://doi.org/10.1016/j.jallcom.2022.167819>.
- [10] Y. Cao, D. Wang, Y. Lin, W. Liu, L. Cao, X. Liu, W. Zhang, X. Mou, S. Fang, X. Shen, T. Yao, Single Pt atom with highly vacant d-orbital for accelerating photocatalytic H₂ evolution, *ACS Appl. Energy Mater.* 1 (2018) 6082–6088, <https://doi.org/10.1021/acsaem.8b01143>.
- [11] X. Zhang, J. Guo, P. Guan, C. Liu, H. Huang, F. Xue, X. Dong, S.J. Pennycook, M. F. Chisholm, Catalytically active single-atom niobium in graphitic layers, *Nat. Commun.* 4 (2013) 1924, <https://doi.org/10.1038/ncomms2929>.
- [12] S. Cao, M. Yang, A.O. Elnabawy, A. Trimpalis, S. Li, C. Wang, F. Goltz, Z. Chen, J. Liu, J. Shan, M. Li, T. Haas, K.W. Chapman, S. Lee, L.F. Allard, M. Mavrikakis, M. Flytzani-Seriopoulos, Single-atom gold oxo-clusters prepared in alkaline solutions catalyse the heterogeneous methanol self-coupling reactions, *Nat. Chem.* 11 (2019) 1098–1105, <https://doi.org/10.1038/s41557-019-0345-3>.
- [13] D. Ghosh, G. Periyasamy, B. Pandey, S.K. Pati, Computational studies on magnetism and the optical properties of transition metal embedded graphitic carbon nitride sheets, *J. Mater. Chem. C* 2 (2014) 7943–7951, <https://doi.org/10.1039/c4tc01385a>.
- [14] B.-B. Xu, X.-B. Fu, X.-M. You, E. Zhao, F.-F. Li, Z. Chen, Y.-X. Li, X.L. Wang, Y.-F. Yao, Synergistic promotion of single-atom Co surrounding a PtCo alloy based on a g-C₃N₄ nanosheet for overall water splitting, *ACS Catal.* 12 (2022) 6958–6967, <https://doi.org/10.1021/acscatal.2c00751>.
- [15] S. Wang, J.-J. Zhang, M.-Y. Zong, J. Xu, D.-H. Wang, X.-H. Bu, Energy level engineering: Ru single atom anchored on Mo-MOF with a [Mo₈O₂₆(im)₂]⁴⁻ structure acts as a biomimetic photocatalyst, *ACS Catal.* 12 (2022) 7960–7974, <https://doi.org/10.1021/acscatal.2c01756>.
- [16] S.L. Li, H. Yin, X. Kan, L.Y. Gan, U. Schwingenschlogl, Y. Zhao, Potential of transition metal atoms embedded in buckled monolayer g-C₃N₄ as single-atom catalysts, *Phys. Chem. Chem. Phys.* 19 (2017) 30069–30077, <https://doi.org/10.1039/c7cp05195f>.
- [17] M. Zhou, G. Dong, J. Ma, F. Dong, C. Wang, J. Sun, Photocatalytic removal of NO by intercalated carbon nitride: the effect of group IIA element ions, *Appl. Catal. B Environ.* 273 (2020), 119007, <https://doi.org/10.1016/j.apcatb.2020.119007>.
- [18] J. Luo, G. Dong, Y. Zhu, Z. Yang, C. Wang, Switching of semiconducting behavior from n-type to p-type induced high photocatalytic NO removal activity in g-C₃N₄, *Appl. Catal. B Environ.* 214 (2017) 46–56, <https://doi.org/10.1016/j.apcatb.2017.05.016>.
- [19] D. Tang, C. Shao, S. Jiang, C. Sun, S. Song, Graphitic C₂N₃: an allotrope of g-C₃N₄ containing active azide pentagons as metal-free photocatalyst for abundant H₂ bubble evolution, *ACS Nano* 15 (2021) 7208–7215, <https://doi.org/10.1021/acsnano.1c00477>.
- [20] Z. Tong, D. Yang, Z. Li, Y. Nan, F. Ding, Y. Shen, Z. Jiang, Thylakoid-inspired multishell g-C₃N₄ nanocapsules with enhanced visible-light harvesting and electron transfer properties for high-efficiency photocatalysis, *ACS Nano* 11 (2017) 1103–1112, <https://doi.org/10.1021/acsnano.6b08251>.
- [21] G. Liu, Y. Huang, H. Lv, H. Wang, Y. Zeng, M. Yuan, Q. Meng, C. Wang, Confining single-atom Pd on g-C₃N₄ with carbon vacancies towards enhanced photocatalytic NO conversion, *Appl. Catal. B Environ.* 284 (2021), 119683, <https://doi.org/10.1016/j.apcatb.2020.119683>.
- [22] B. Qiao, A. Wang, X. Yang, L.F. Allard, Z. Jiang, Y. Cui, J. Liu, J. Li, T. Zhang, Single-atom catalysis of CO oxidation using Pt1/FeOx, *Nat. Chem.* 3 (2011) 634–641, <https://doi.org/10.1038/nchem.1095>.
- [23] L. Han, H. Cheng, W. Liu, H. Li, P. Ou, R. Lin, H.T. Wang, C.W. Pao, A.R. Head, C. H. Wang, X. Tong, C.J. Sun, W.F. Wong, J. Luo, J.C. Zheng, H.L. Xin, A single-atom library for guided monometallic and concentration-complex multimetallic designs, *Nat. Mater.* 21 (2022) 681–688, <https://doi.org/10.1038/s41563-022-01252-y>.
- [24] S. Shen, X. Xia, Y. Zhong, S. Deng, D. Xie, B. Liu, Y. Zhang, G. Pan, X. Wang, J. Tu, Implanting niobium carbide into trichoderma spore carbon: a new advanced host for sulfur cathodes, *Adv. Mater.* 31 (2019), e1900009, <https://doi.org/10.1002/adma.201900009>.
- [25] Y. Xue, Y. Lei, X. Liu, Y. Li, W. Deng, F. Wang, S. Min, Highly active dye-sensitized photocatalytic H₂ evolution catalyzed by a single-atom Pt cocatalyst anchored onto g-C₃N₄ nanosheets under long-wavelength visible light irradiation, *New J. Chem.* 42 (2018) 14083–14086, <https://doi.org/10.1039/c8nj02933d>.
- [26] Q. Chen, G. Gao, Y. Zhang, Y. Li, H. Zhu, P. Zhu, Y. Qu, G. Wang, W. Qin, Dual functions of CO₂ molecular activation and 4f levels as electron transport bridges in erbium single atom composite photocatalysts therefore enhancing visible-light photoactivities, *J. Mater. Chem. A* 9 (2021) 15820–15826, <https://doi.org/10.1039/d1ta02926f>.
- [27] Y. Li, B. Li, D. Zhang, L. Cheng, Q. Xiang, Crystalline carbon nitride supported copper single atoms for photocatalytic CO₂ reduction with nearly 100% CO selectivity, *ACS Nano* 14 (2020) 10552–10561, <https://doi.org/10.1021/acsnano.0c04544>.
- [28] K. Wang, Y. Li, J. Li, G. Zhang, Boosting interfacial charge separation of Ba₂Nb₄O₁₅/g-C₃N₄ photocatalysts by 2D/2D nanojunction towards efficient visible-light driven H₂ generation, *Appl. Catal. B Environ.* 263 (2020), 117730, <https://doi.org/10.1016/j.apcatb.2019.05.032>.
- [29] Y. Wang, L. Rao, P. Wang, Z. Shi, L. Zhang, Photocatalytic activity of N-TiO₂/O-doped N vacancy g-C₃N₄ and the intermediates toxicity evaluation under tetracycline hydrochloride and Cr(VI) coexistence environment, *Appl. Catal. B Environ.* 262 (2020), 118308, <https://doi.org/10.1016/j.apcatb.2019.118308>.
- [30] Y. Tan, W. Chen, G. Liao, X. Li, J. Wang, Y. Tang, L. Li, Strategy for improving photocatalytic ozonation activity of g-C₃N₄ by halogen doping for water purification, *Appl. Catal. B Environ.* 306 (2022), 121133, <https://doi.org/10.1016/j.apcatb.2022.121133>.
- [31] K. Wu, D. Chen, S. Lu, J. Fang, X. Zhu, F. Yang, T. Pan, Z. Fang, Supramolecular self-assembly synthesis of noble-metal-free (C, Ce) co-doped g-C₃N₄ with porous structure for highly efficient photocatalytic degradation of organic pollutants, *J. Hazard. Mater.* 382 (2020), 121027, <https://doi.org/10.1016/j.jhazmat.2019.121027>.
- [32] M. Wang, Y. Zeng, G. Dong, C. Wang, Br-doping of g-C₃N₄ towards enhanced photocatalytic performance in Cr(VI) reduction, *Chin. J. Catal.* 41 (2020) 1498–1510, [https://doi.org/10.1016/s1872-2067\(19\)63435-2](https://doi.org/10.1016/s1872-2067(19)63435-2).
- [33] H. Jiang, C. Zang, Y. Zhang, W. Wang, C. Yang, B. Sun, Y. Shen, F. Bian, 2D MXene-derived Nb₂O₅/C/Nb₂C/g-C₃N₄ heterojunctions for efficient nitrogen photofixation, *Catal. Sci. Technol.* 10 (2020) 5964–5972, <https://doi.org/10.1039/d0cy00656d>.
- [34] T. Wang, G. Yu, J. Liu, X. Huang, W. Chen, Theoretical design of a series of 2D TM-C₃N₄ and TM-C₃N₄@graphene (TM = V, Nb and Ta) nanostructures with highly efficient catalytic activity for the hydrogen evolution reaction, *Phys. Chem. Chem. Phys.* 21 (2019) 1773–1783, <https://doi.org/10.1039/c8cp06011h>.
- [35] S. Wang, F. He, X. Zhao, J. Zhang, Z. Ao, H. Wu, Y. Yin, L. Shi, X. Xu, C. Zhao, S. Wang, H. Sun, Phosphorous doped carbon nitride nanobelts for photodegradation of emerging contaminants and hydrogen evolution, *Appl. Catal. B Environ.* 257 (2019), 117931, <https://doi.org/10.1016/j.apcatb.2019.117931>.
- [36] J. Luo, H. Han, X. Wang, Y. Lai, B. Liu, R. Zhong, Y. Zhang, S. Zhang, L. Wang, Constructing oxygen absorption and activation sites in Ce-doped g-C₃N₄ photocatalyst for effective removal of amoxicillin: performance, mechanism and degradation pathways, *Appl. Surf. Sci.* 611 (2023), 155808, <https://doi.org/10.1016/j.apsusc.2022.155808>.
- [37] H. Zhang, P. Zhang, J. Zhao, Y. Liu, Y. Huang, H. Huang, C. Yang, Y. Zhao, K. Wu, X. Fu, S. Jin, Y. Hou, Z. Ding, R. Yuan, M.B.J. Roefaaers, S. Zhong, J. Long, The hole-tunneling heterojunction of hematite-based photoanodes accelerates photosynthetic reaction, *Angew. Chem. Int. Ed. Engl.* 60 (2021) 16009–16018, <https://doi.org/10.1002/anie.202102983>.
- [38] C. Lin, J.-L. Li, X. Li, S. Yang, W. Luo, Y. Zhang, S.-H. Kim, D.-H. Kim, S.S. Shinde, Y.-F. Li, Z.-P. Liu, Z. Jiang, J.-H. Lee, n-situ reconstructed Ru atom array on α -MnO₂ with enhanced performance for acidic water oxidation, *Nat. Catal.* 4 (2021) 1012–1023, <https://doi.org/10.1038/s41929-021-00703-0>.
- [39] K. Qi, X. Cui, L. Gu, S. Yu, X. Fan, M. Luo, S. Xu, N. Li, L. Zheng, Q. Zhang, J. Ma, Y. Gong, F. Lv, K. Wang, H. Huang, W. Zhang, S. Guo, W. Zheng, P. Liu, Single-atom cobalt array bound to distorted 1T MoS₂ with ensemble effect for hydrogen evolution catalysis, *Nat. Commun.* 10 (2019) 5231, <https://doi.org/10.1038/s41467-019-12997-7>.
- [40] X. Hai, S. Xi, S. Mitchell, K. Harrath, H. Xu, D.F. Akl, D. Kong, J. Li, Z. Li, T. Sun, H. Yang, Y. Cui, C. Su, X. Zhao, J. Li, J. Perez-Ramirez, J. Lu, Scalable two-step annealing method for preparing ultra-high-density single-atom catalyst libraries, *Nat. Nanotechnol.* 17 (2022) 174–181, <https://doi.org/10.1038/s41565-021-01022-y>.
- [41] K. Sun, K. Yu, J. Fang, Z. Zhuang, X. Tan, Y. Wu, L. Zeng, Z. Zhuang, Y. Pan, C. Chen, Nature-inspired design of molybdenum-selenium dual-single-atom electrocatalysts for CO₂ reduction, *Adv. Mater.* (2022), e2206478, <https://doi.org/10.1002/adma.202206478>.
- [42] J. San Martin, N. Dang, E. Raulerson, M.C. Beard, J. Hartenberger, Y. Yan, Perovskite photocatalytic CO₂ reduction or photoredox organic transformation? *Angew. Chem. Int. Ed. Engl.* (2022), e202205572 <https://doi.org/10.1002/anie.202205572>.
- [43] J. Zhou, D. Li, W. Zhao, B. Jing, Z. Ao, T. An, First-principles evaluation of volatile organic compounds degradation in Z-scheme photocatalytic systems: MXene and graphitic-C₃N₄ heterostructures, *ACS Appl. Mater. Interfaces* 13 (2021) 23843–23852, <https://doi.org/10.1021/acsami.1c05617>.
- [44] W. Jiang, Y. Zhao, X. Zong, H. Nie, L. Niu, L. An, D. Qu, X. Wang, Z. Kang, Z. Sun, Photocatalyst for high-performance H₂ production: Ga-doped polymeric carbon nitride, *Angew. Chem. Int. Ed. Engl.* 60 (2021) 6124–6129, <https://doi.org/10.1002/anie.202015779>.
- [45] M. Zhou, G. Dong, F. Yu, Y. Huang, The deep oxidation of NO was realized by Sr multi-site doped g-C₃N₄ via photocatalytic method, *Appl. Catal. B Environ.* 256 (2019), 117825, <https://doi.org/10.1016/j.apcatb.2019.117825>.
- [46] X. Zhang, P. Ma, C. Wang, L. Gan, X. Chen, P. Zhang, Y. Wang, H. Li, L. Wang, X. Zhou, K. Zheng, Unraveling the dual defect sites in graphite carbon nitride for ultra-high photocatalytic H₂O₂ evolution, *Energy Environ. Sci.* 15 (2022) 830–842, <https://doi.org/10.1039/d1ee02369a>.
- [47] C. Zhang, D. Qin, Y. Zhou, F. Qin, H. Wang, W. Wang, Y. Yang, G. Zeng, Dual optimization approach to Mo single atom dispersed g-C₃N₄ photocatalyst: morphology and defect evolution, *Appl. Catal. B Environ.* 303 (2022), 120904, <https://doi.org/10.1016/j.apcatb.2021.120904>.
- [48] Y. Zhou, C. Zhang, D. Huang, W. Wang, Y. Zhai, Q. Liang, Y. Yang, S. Tian, H. Luo, D. Qin, Structure defined 2D Mo₂C/2Dg-C₃N₄ Van der Waals heterojunction: oriented charge flow in-plane and separation within the interface to collectively promote photocatalytic degradation of pharmaceutical and personal care products, *Appl. Catal. B Environ.* 301 (2022), 120749, <https://doi.org/10.1016/j.apcatb.2021.120749>.
- [49] M. Yang, P. Wang, Y. Li, S. Tang, X. Lin, H. Zhang, Z. Zhu, F. Chen, Graphene aerogel-based NiAl-LDH/g-C₃N₄ with ultrathin sheet-sheet heterojunction for excellent visible-light photocatalytic activity of CO₂ reduction, *Appl. Catal. B Environ.* 306 (2022), 121065, <https://doi.org/10.1016/j.apcatb.2022.121065>.

- [50] H. Shi, H. Wang, Y. Zhou, J. Li, P. Zhai, X. Li, G.G. Gurzadyan, J. Hou, H. Yang, X. Guo, Atomically dispersed indium-copper dual-metal active sites promoting C-C coupling for CO₂ photoreduction to ethanol, *Angew. Chem. Int. Ed. Engl.* (2022), e202208904, <https://doi.org/10.1002/anie.202208904>.
- [51] H. Ou, S. Ning, P. Zhu, S. Chen, A. Han, Q. Kang, Z. Hu, J. Ye, D. Wang, Y. Li, Carbon nitride photocatalysts with integrated oxidation and reduction atomic active centers for improved CO₂ conversion, *Angew. Chem. Int. Ed. Engl.* 61 (2022), e202206579, <https://doi.org/10.1002/anie.202206579>.
- [52] Y. Zhao, L. Wang, R. Malpass-Evans, N.B. McKeown, M. Carta, J.P. Lowe, C.L. Lyall, R. Castaing, P.J. Fletcher, G. Kociok-Kohn, J. Wenk, Z. Guo, F. Marken, Effects of g-C₃N₄ heterogenization into intrinsically microporous polymers on the photocatalytic generation of hydrogen peroxide, *ACS Appl. Mater. Interfaces* 14 (2022) 19938–19948, <https://doi.org/10.1021/acsami.1c23960>.
- [53] H. Zhan, Q. Zhou, M. Li, R. Zhou, Y. Mao, P. Wang, Photocatalytic O₂ activation and reactive oxygen species evolution by surface B-N bond for organic pollutants degradation, *Appl. Catal. B Environ.* 310 (2022), 121329, <https://doi.org/10.1016/j.apcatb.2022.121329>.
- [54] K. Wang, L. Jiang, T. Xin, Y. Li, X. Wu, G. Zhang, Single-atom V-N charge-transfer bridge on ultrathin carbon nitride for efficient photocatalytic H₂ production and formaldehyde oxidation under visible light, *Chem. Eng. J.* 429 (2022), 132229, <https://doi.org/10.1016/j.cej.2021.132229>.
- [55] Q. Zhu, R. Hailili, Y. Xin, Y. Zhou, Y. Huang, X. Pang, K. Zhang, P.K.J. Robertson, D.W. Bahnemann, C. Wang, Efficient full spectrum responsive photocatalytic NO conversion at Bi₂Ti₂O₇: Co-effect of plasmonic Bi and oxygen vacancies, *Appl. Catal. B Environ.* 319 (2022), 121888, <https://doi.org/10.1016/j.apcatb.2022.121888>.
- [56] D. Zhou, X. Xue, X. Wang, Q. Luan, A. Li, L. Zhang, B. Li, W. Dong, G. Wang, C. Hou, Ni, In co-doped ZnIn₂S₄ for efficient hydrogen evolution: modulating charge flow and balancing H adsorption/desorption, *Appl. Catal. B Environ.* 310 (2022), <https://doi.org/10.1016/j.apcatb.2022.121337>.
- [57] J. Luo, H. Han, J. Wu, X. Wang, J. Feng, S. Toan, L. Wang, Y. Lai, Excellent photocatalytic activity of MoO₃-adorned g-C₃N₄ systems: construction of S-scheme heterojunction, *Appl. Surf. Sci.* 604 (2022), 154512, <https://doi.org/10.1016/j.apsusc.2022.154512>.
- [58] X. Bai, Q. Hou, H. Qian, Y. Nie, T. Xia, R. Lai, G. Yu, M. Laiq Ur Rehman, H. Xie, M. Ju, Selective oxidation of glucose to gluconic acid and glucaric acid with chlorin e6 modified carbon nitride as metal-free photocatalyst, *Appl. Catal. B Environ.* 303 (2022), 120895, <https://doi.org/10.1016/j.apcatb.2021.120895>.
- [59] J. Yu, Q. Liu, W. Qiao, D. Lv, Y. Li, C. Liu, Y. Yu, Y. Li, H. Niemantsverdriet, B. Zhang, R. Su, Catalytic role of metal nanoparticles in selectivity control over photodehydrogenative coupling of primary amines to imines and secondary amines, *ACS Catal.* 11 (2021) 6656–6661, <https://doi.org/10.1021/acscatal.1c01519>.